Locally Optimal Periods in Periodic Optically Transparent Two-Metal-Layered Refractive Metasurfaces for Outdoor-to-Indoor Communication

Byeongjin Kim, *Graduate Student Member, IEEE,* Seungwoo Bang, *Graduate Student Member, IEEE,* Sunghyun Kim, Doyle Kwon, Seongkwan Kim, and Jungsuek Oh, *Senior Member, IEEE*

***Abstract*—This study presents a novel electromagnetic analysis and mathematical derivation for determining the locally optimal unit cell period that minimizes phase error losses in the macroscopic design of a periodic two-metal-layered refractive metasurface (TRM) for outdoor-to-indoor (O2I) communication. The TRM's periodicity is investigated for three main advantages: reducing design complexity, lowering lifecycle costs, and increasing area efficiency. The existence of locally optimal unit cell periods for each pair of incidence and refraction angles, along with a method to find them, was derived. Finally, a 6G upper-mid optically transparent TRM with a locally optimal unit cell period was fabricated, and its path losses in both far-field and near-field scenarios were measured to validate the proposed technique.**

***Index Terms*—Periodicity, Metasurface, 6G Upper-mid, Outdoor-to-Indoor, Optically Transparent.**

I. Introduction

RECENTLY, the reconfigurable intelligent surfaces (RISs), has emerged as an attractive tool for enhancing outdoor-to-outdoor communication [1]- [9]. Unlike previous metasurfaces [10], [11], RISs can redirect incident waves, creating robust signal paths in non-line-of-sight (NLOS) scenarios. However, for outdoor-to-indoor (O2I) communication, transmissive metasurfaces cannot be applied to walls or frames of buildings and vehicles due to high insertion losses [12]. Instead, optically transparent transmissive metasurfaces must be printed on glass windows [13]- [26], which complicates the adoption of tunable elements. Additionally, incorporating three or more metal layers into the design of the refractive metasurface (RM) increases complexity. Therefore, this paper focuses on a passive-type two-metal-layered RM (TRM), despite its limited unit cell phase tuning range of approximately 180° within a 3 dB transmission loss threshold [27].

Since the TRM experiences phase error loss (PEL) due to its limited unit cell phase tunable range, design techniques to reduce PEL are urgently needed. In [28], the effect of a limited phase range on the gain and bandwidth of a multi-layered transmitarray is demonstrated. In [29], particle swarm optimization is applied to address the constrained phase range of 255° in the design of a three-metal-layered transmitarray. In [20], the tunable phase range of a TRM unit cell was extended to 220° by permitting a unit cell transmission loss of up to 7.7 dB. However, despite achieving a wide beam refraction angle range, severe refraction losses occurred, exceeding 10 dB at oblique incidence.

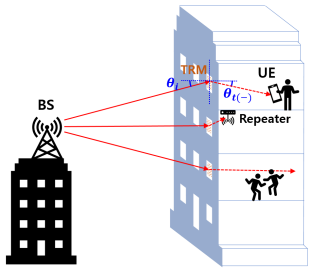

Fig. 1. Illustration of outdoor-to-indoor (O2I) communication enhanced by optically transparent two-metal-layered refractive metasurfaces (TRMs), involving adaptive base stations (BSs), user equipment (UE), and repeaters.

This paper highlights three key advantages of periodic TRMs. First, they reduce design complexity by minimizing optimization parameters and enabling faster validation through Floquet simulations on unit cell subarrays, avoiding time-intensive simulations of the entire TRM. Second, they lower lifecycle costs by facilitating modular fabrication with small photomasks and allowing for individual block replacement instead of replacing the whole TRM. Finally, they increase area efficiency by using smaller unit cell subarrays to maximize coverage, reduce void fractions, and enhance packing density, directly improving the refracted power proportional to the TRM's area.

We present a novel electromagnetic analysis and mathematical derivation for the locally optimal unit cell periods that minimize PEL in the macroscopic design of periodic TRMs, utilizing antenna array theory and the pattern search algorithm. A 6G upper-mid optically transparent TRM with a locally optimal unit cell period is fabricated as an example, and its far-field and near-field path losses are measured to validate the proposed derivation. This paper is a substantially enhanced version of the authors' previous conference paper [30].

Manuscript created January, 2024.

This work was supported in part by KT Corporation, and in part by an Institute of Information Communications Technology Planning Evaluation (IITP) grant funded by the Korean government (MSIT) under Grant 2020-0-00858 (Millimeter-wave Metasurface-based Dualband Beamforming Antenna-on-Package Technology for 5G Smartphone). (Corresponding author: Jungsuek Oh.). (Corresponding author: Jungsuek Oh.).

Byeongjin Kim, Seungwoo Bang, and Jungsuek Oh are affiliated with the Institute of New Media and Communications (INMC), Department of Electrical and Computer Engineering, Seoul National University, Seoul 08826, South Korea (e-mail: jungsuek@snu.ac.kr).

Sunghyun Kim, Doyle Kwon, and Seongkwan Kim are with KT Corporation, Seoul, South Korea.

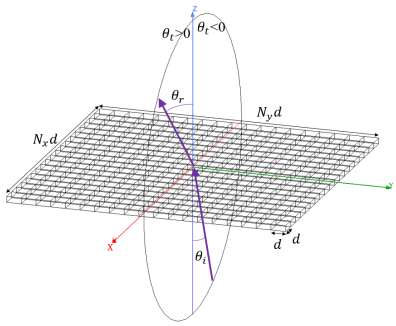

Fig. 2. Illustration of an electromagnetic wave ray transmitted with incidence and refraction angles θ_i and θ_r through an RM with $N_x \times N_y$ unit cells, each of size $d \times d$.

II. Phase Error Factor and Loss of the TRM

Initially, we consider the incident wave on the RM to be a plane wave in the context of O2I communication. This assumption arises from the typical positioning of outdoor base stations (BS) or user equipment (UE), which are expected to be located in the far field relative to the glass window, as shown in Fig. 1. For simplicity, this paper focuses on 1-D refraction, where the incident and transmitted wave rays are assumed to lie in the same xz-plane without azimuthal rotation. The phase tunable range of the TRM unit cell is limited to 180° for a 3 dB transmission loss threshold [27].

To illustrate how to calculate PEL, consider an RM composed of $N_x \times N_y$ unit cells with each unit cell sized $d \times d$, as shown in Fig. 2. Thus, the RM aperture area $A = N_x N_y d^2$. The RM array gain A_G for arbitrary incidence and refraction angles, θ_i and θ_r can be calculated as follows:

$$A_G(\theta_i, \theta_r) = E_G(\theta_r) \times |AF(\theta_i, \theta_r)|^2, \tag{1}$$

where E_G and AF are defined as the unit cell gain and array factor, respectively, and they can be calculated as follows:

$$E_G(\theta_r) = e_r \frac{4\pi d^2}{\lambda^2} \times \cos^{2q}\theta_r, \tag{2}$$

$$AF(\theta_i, \theta_r) = N_y \times \Sigma_{n=1}^{N_x} a_n(\theta_i) \exp(jnkd \sin\theta_r), \tag{3}$$

where e_r is defined as the unit cell radiation efficiency, the $\cos^q$ pattern is adopted for simplicity [31], and $a_n(\theta_i)$ is defined as the complex-valued excitation coefficient for each unit cell, with a magnitude of $1/\sqrt{N_x N_y}$. k and λ are the free-space wave number and wavelength, respectively. Defining ϕ_n as the phase tuned by the n-th unit cell when the wave is transmitted through it, $a_n(\theta_i)$ can be calculated as follows:

$$a_n(\theta_i) = \frac{1}{\sqrt{N_X N_y}} \exp(-jnkd \sin\theta_i + j\phi_n). \tag{4}$$

Through equations (1)-(4), it is derived that $A_G(\theta_i, \theta_r)$ has a maximal value if ϕ_n $(n = 1 \sim N_x)$ is assigned as follows:

$$\phi_{n,ideal} = nkd(\sin\theta_i - \sin\theta_r), \tag{5}$$

$$A_{G,max}(\theta_i, \theta_r) = e_r \frac{4\pi A}{\lambda^2} \times \cos^{2q}\theta_r. \tag{6}$$

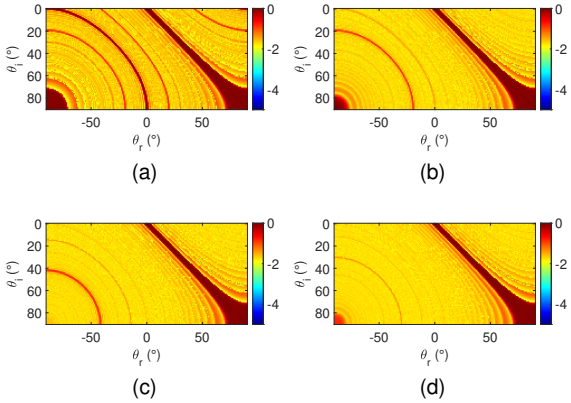

Fig. 3. The optimized *PEF* of aperiodic TRMs in dB scale for arbitrary θ_i and θ_r pairs, with kd (or d) equal to (a) π (or $\lambda/2$), (b) $\pi/2$ (or $\lambda/4$), (c) $2\pi/5$ (or $\lambda/5$), and (d) $\pi/3$ (or $\lambda/6$). The values of N_x are 30, 60, 75, and 90, respectively.

The ideal phase tuning difference between consecutive unit cells can be easily derived from (5) as follows:

$$\Delta\phi_{ideal} = \phi_{(i+1),ideal} - \phi_{(i),ideal} = kd(\sin\theta_i - \sin\theta_r). \tag{7}$$

The TRM unit cells, with their limited phase tunable range, cannot satisfy equations (5)-(7). In this paper, the phase error factor (*PEF*) and PEL are defined as follows:

$$PEF = \frac{A_G(\theta_i, \theta_r)}{A_{G,max}(\theta_i, \theta_r)} \tag{8}$$

$$= \frac{|\Sigma_{n=1}^{N_x} \exp(jnkd(\sin\theta_r - \sin\theta_i) + j\phi_n)|^2}{N_x^2}, \tag{9}$$

$$PEL|_{dB} = \frac{1}{PEF}|_{dB} = -10\log_{10} PEF, \tag{10}$$

where *PEF* on a linear scale has its value between 0 and 1, and PEL is the inverse of *PEF*.

III. Optimization of Aperiodic TRM

A. Optimal Unit Cell Phase Tuning Set: ϕ_n

The pattern search algorithm (PSA), known for its high accuracy and short running time, is employed to find the optimal values of ϕ_n $(n = 1 \sim N_x)$ that minimize the PEL of the TRM. In this process, PEL is designated as the cost function to be minimized:

$$Cost = PEL(N_x, kd, \theta_i, \theta_r, \phi_n). \tag{11}$$

After the optimization of ϕ_n, the minimized PEL for the periodic TRM becomes a function of two parameters: N_x and kd. Since N_x is determined based on the specific application, kd must be optimized to further minimize the PEL.

B. Optimal Unit Cell Size: d

Fig. 3 shows the optimized *PEF* of TRMs with variations in unit cell size, d. All other parameters were kept constant except for N_x, to maintain an equal TRM aperture area A, ensuring an equal $A_{G,max}$ from (6) for a fair comparison. The average PEL decreases as d increases, which goes against our

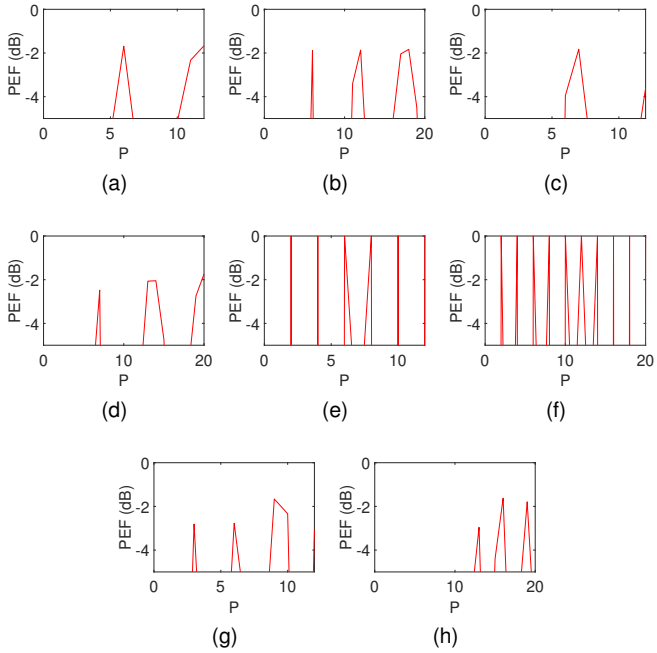

Fig. 4. The optimized *PEF* of periodic TRMs in dB scale with variation in unit cell period P, when $(\theta_i, \theta_r, N_x)$ is equal to (a) $(0°, 20°, 24)$, (b) $(0°, 20°, 40)$, (c) $(20°, 40°, 24)$, (d) $(20°, 40°, 40)$, (e) $(30°, -30°, 24)$, (f) $(30°, -30°, 40)$, (g) $(30°, -60°, 24)$, (h) $(30°, -60°, 40)$. $kd = \pi$.

intuition since a smaller unit cell size typically leads to higher phase resolution. We attribute this counterintuitive result to the limited phase tunable range of TRM unit cells. However, when d exceeds $\lambda/2$, undesired grating lobes emerge, meaning that d cannot exceed $\lambda/2$ [32]. Therefore, the optimal TRM unit cell size is half a wavelength.

IV. Optimal Unit Cell Period for Periodic TRM

In this section, we advance the design of the TRM by incorporating periodicity, where $\phi_{i+P} = \phi_i$. The unit cell period P is now included as a parameter in the cost function (11) for optimization. The value $d = \lambda/2$, derived for the aperiodic TRM, is also selected for the periodic TRM.

Fig. 4 illustrates examples of how the *PEF* varies with changes in P. The value of P was limited to $N_x/2$ to ensure at least two periods are arranged. Notably, we find that the PEL does not decrease as P increases for the same N_x. Instead, there are unique values of P for each (θ_i, θ_r) pair that locally minimize the PEL. For example, we observe a unique minimal P value, P_{min}, for each (θ_i, θ_r) pair that results in a small PEL of less than 3 dB: $P_{\text{min}} = 6, 7, 2$, and 3 for $(\theta_i, \theta_r) = (0°, 20°)$, $(20°, 40°)$, $(30°, -30°)$, and $(30°, -60°)$, respectively. The higher P values that produce local minimal PELs are close to multiples of P_{min}. These P values were found to satisfy the following condition:

$$\frac{\Delta\phi_{ideal}}{2\pi}(P - \frac{P^\alpha}{N_x}) \leq Z \leq \frac{\Delta\phi_{ideal}}{2\pi}(P + \frac{P^\alpha}{N_x}), \quad (12)$$

where Z represents an arbitrary positive integer, $\Delta\phi_{ideal}$ is defined in (7), and α is manually fitted as follows:

$$\alpha = 0.88 \times |\sin\theta_i - \sin\theta_r|^{-0.4}. \quad (13)$$

Equation (12) successfully estimates the P values for most (θ_i, θ_r) pairs, including the examples shown in Fig. 4, with the exception of pairs close to $(0°, 0°)$ and $(90°, -90°)$. A reference PEL of 3 dB was used for this estimation. However, if the reference PEL is set to be less than 3 dB, then both the coefficient and exponent of α in equation (13) should decrease, resulting in a lower α value and providing a stricter condition for P to satisfy equation (12) with the modified equation (13).

V. Fabrication and Experimental Results

A. Measurement of PEF of TRM

The *PEF* can be indirectly measured and validated by measuring path losses in TRM-aided NLOS scenarios. Simple yet sufficiently accurate far-field and near-field path loss models for the RM can be derived from the path loss models for reflective-type RISs outlined in [7], as follows:

$$PL_{far-field} = \frac{(4\pi r_{tT} r_{rT})^2}{G_t G_r N_{tot}^2 A_{UC}^2 \cos\theta_i \cos\theta_r |T|^2 PEF}, \quad (14)$$

$$PL_{near-field} = \frac{(4\pi(r_{tT} + r_{rT}))^2}{G_t G_r \lambda^2 |T|^2 PEF}, \quad (15)$$

where r_{tT}, r_{rT}, G_t, G_r, N_{tot}, A_{UC}, and T are defined as the distance between the transmitting antenna (Tx) and the RM, the distance between the receiving antenna (Rx) and the RM, the Tx gain, the Rx gain, the total number of unit cells on the RM aperture, the physical area of the RM unit cell, and the average magnitude of the transmission coefficient of the RM unit cell, respectively.

B. TRM Design and Fabrication for Proof-of-Derivation

A TRM designed with the optimal unit cell period for a 12 GHz TM mode in the 6G upper-mid band application is fabricated and measured in both far-field and near-field environments. The configuration used for the measurements is $(\theta_i, \theta_r, d, P, N_x) = (30°, -60°, \frac{\lambda}{2}, 3, 24)$. The unit cell size is 12.5 mm×12.5 mm ($\lambda/2 \times \lambda/2$), and the total aperture size is 300 mm×300 mm ($12\lambda \times 12\lambda$). Fabrication was performed using photolithography on two glass substrates, each measuring 370 mm × 470 mm, with a dielectric constant of 5.27 and a loss tangent of 0.003. The two metal layers of the TRM were printed separately on the two glass substrates, which were then aligned and positioned facing each other with a 4 mm air gap. The air gap was maintained with a margin of error of only 0.2 mm (5% error rate) using a specially designed jig, fabricated in-house with a high-resolution 3D printer. The 500 nm-thick copper metal layers, with a conductivity of 5.8×10^7 S/m, were deposited onto the glass substrates using photolithography and precisely aligned using the jig. This process ensured the alignment of the TRM unit cells with an error rate of only 1.6%.

The target TRM is designed with a locally optimal period P value of 3, determined using equation (12) to calculate the optimal unit cell period. The corresponding ideal phase set of $[180°, 90°, 0°]$ is derived from Section III. The double-ring unit cell (DRUC) shown in Fig. 5(a) is selected as an example due to its double-resonance capability, which enables

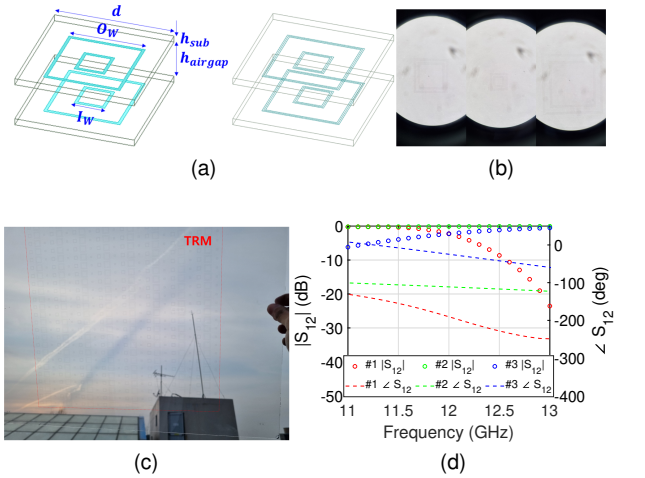

Fig. 5. (a) Illustration of the fabricated TRM unit cell type and its optically transparent version; photographs of (b) unit cells enlarged using a microscope and (c) the fabricated optically transparent TRM sample; (d) the transmission response of the selected unit cells. The dimensions are $(d, h_{sub}, h_{airgap}) = (12.5, 0.7, 4)$, and $(O_w, I_w) = (6, 4.5), (3, 1.95)$, and $(10, 8)$ for unit cells #1, 2, and 3, respectively (units: mm).

achieving the theoretically maximum transmission phase range of 180° [27]. The opaque DRUC is converted into an optically transparent mesh-grid form by replacing each opaque ring with three concentric, ultra-thin (10 μm) rings with a line spacing of 0.15 mm, achieving a similar transmission response while attaining a calculated optical transparency (OT) of 99.15% [33]. Photographs of the fabricated optically transparent TRM sample confirm its high OT, as shown in Fig. 5(b) and Fig. 5(c). Fig. 5(d) illustrates the transmittance response of three selected DRUCs. A scan angle of 30° ($= \theta_i$) was applied in the simulation setup. From the selected DRUCs, a phase set of $[-25°, -111°, 170°]$, or $[175°, 89°, 10°]$ when normalized, is obtained. Although Fig. 5(d) shows that Unit Cells #1 and #3 exhibit relatively low transmission in the upper and lower bands, respectively, the proposed TRM performs effectively in these bands due to its wider transmission phase range or the tolerable transmission levels within the overall TRM performance. To improve unit cell bandwidth, additional metal layers beyond two can be employed [27], [34], but this comes at the expense of reduced optical transparency [24].

To apply equations (14) and (15), $|T|$ and *PEF* values need to be calculated. First, $|T|$ is computed as the average transmission magnitude of unit cells #1, #2, and #3, resulting in a value of 0.8422, or -1.4914 dB. For the ideal TRM phase set $[180°, 90°, 0°]$ and the selected phase set $[175°, 89°, 10°]$, the *PEF* is calculated to be 0.5238 and 0.4790, respectively. It is evident that the *PEF* equals 1 (i.e., $PEL = 0$) for an ideal RM with a unit cell phase tunable range of 360°.

C. Far-Field and Near-Field Measurements

Fig. 6 illustrates the setup for both rooftop and anechoic chamber environments used for far-field and near-field measurements, respectively. In the path loss equations (14) and (15), G_t, G_r, N_{tot}, A_{UC}, and λ are 16 dBi, 16 dBi, 576, 156.25 mm^2, and 25 mm, respectively. For far-field measurements, r_{tT} and r_{rT} are set at 7.5 m and 7.5-15 m, respectively, while for near-field measurements, these distances are 0.8 m and 1-3.5 m, respectively. X-band horn antennas were used as the Tx and Rx. The transmitted power P_t is 20 dBm for far-field measurements and 0 dBm for near-field measurements, supplied by a signal generator.

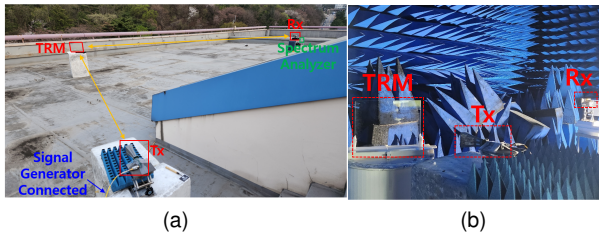

Fig. 6. Measurement setups: (a) rooftop of the building for far-field measurements and (b) RF anechoic chamber for near-field measurements.

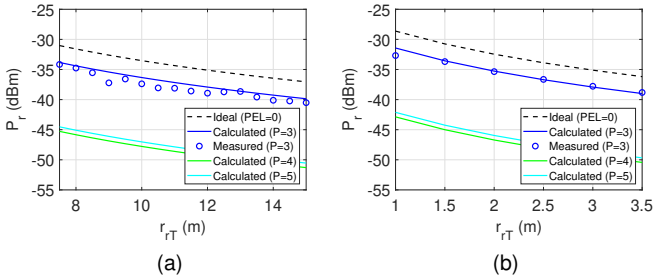

Fig. 7. The calculated and measured received power, P_r, in (a) far-field and (b) near-field environments at 12 GHz.

Fig. 7 presents the calculated and measured received power for the RM with the ideal phase assignment (PEL=0) and TRMs with unit cell periods $P = 3, 4$, and 5, in both far-field and near-field environments. The calculated and measured results for the designed TRM with the optimally determined unit cell period $P = 3$ show good agreement. The deviation in received power P_r of around 3 dB between the ideal case and $P = 3$ corresponds to the predicted PEL value shown in Fig. 4(g). Minor discrepancies are attributed to assumptions such as treating the incident wave as a plane wave and assuming identical values for r_{tT}, r_{rT}, θ_i, and θ_r for every unit cell of the TRM sample. The calculated results for TRMs with $P = 4$ and $P = 5$ are also provided to highlight the importance of selecting the optimal unit cell period in periodic TRM design, demonstrating that properly choosing P can result in up to 10 dB higher received power for O2I communication.

VI. Conclusion

A novel electromagnetic analysis and mathematical derivation are presented to determine the locally optimal unit cell periods that minimize refraction losses in the macroscopic design of a periodic TRM for O2I communication. Due to the limited phase tunable range of approximately 180°, a PEL is defined, and the locally optimal unit cell periods that minimize PEL are derived for arbitrary incidence and refraction angles. The proposed locally optimal unit cell periods are validated through far-field and near-field path loss measurements.

ACKNOWLEDGMENT

This work was supported by KT Corporation.

REFERENCES

[1] H. Yang *et al.*, "Beyond Limitations of 5G with RIS: Field Trial in a Commercial Network, Recent Advances, and Future Directions," *IEEE Comm. Mag.*, to be published.

[2] H. Kim *et al.*, "Independently Polarization Manipulable Liquid-Crystal-Based Reflective Metasurface for 5G Reflectarray and Reconfigurable Intelligent Surface," *IEEE Trans. Antennas Propag.*, vol. 71, no. 8, pp. 6606-6616, Aug. 2023.

[3] A. Araghi *et al.*, "Reconfigurable intelligent surface (RIS) in the sub-6 GHz band: Design, implementation, and real-world demonstration," *IEEE Access*, vol. 10, pp. 2646–2655, 2022.

[4] X. Pei *et al.*, "RIS-aided wireless communications: Prototyping, adaptive beamforming, and indoor/outdoor field trials," *IEEE Trans. Comm.*, vol. 69, no. 12, pp. 8627–8640, 2021.

[5] J. Sang *et al.*, "Coverage enhancement by deploying RIS in 5G commercial mobile networks: Field trials," *IEEE Wireless Comm.*, 2022.

[6] J. Jeong *et al.*, "An improved path loss model for reconfigurable-intelligent-surface-aided wireless communications and experimental validation," *IEEE Access*, vol. 10, pp. 98 065–98 078, 2022.

[7] W. Tang *et al.*, "Path loss modeling and measurements for reconfigurable intelligent surfaces in the millimeter-wave frequency band," *IEEE Trans. Comm.*, vol. 70, no. 9, pp. 6259–6276, 2022.

[8] J. Kim and I. Hong, "Inverse Design of Electromagnetic Metasurfaces Utilizing Infinite and Separate Latent Space Yielded by a Machine Learning-Based Generative Model," *J. Electromagn. Eng. Sci.*, vol. 24, no. 2, pp. 178-190, Mar. 2024.

[9] H. Jung and J. Lee, "Theoretical and Experimental Investigation of N-Bit Reconfigurable Retrodirective Metasurface," *J. Electromagn. Eng. Sci.*, vol. 24, no. 1, pp. 51-56, Jan. 2024.

[10] B. Kim, J. Jung, S. Yun, H. Kim and J. Oh, "Heterogeneous Metasurface Empowering Proximate High-Permittivity Ceramic Cover for a 5G Dual-Band Millimeter-Wave Smartphone," *IEEE Trans. Antennas Propag.*, vol. 72, no. 5, pp. 4086-4094, May 2024.

[11] S. Bang, T. Yoon, B. Kim, J. Oh, H. Kim and J. Oh, "Extremely Miniaturized Free-Space Measurement System for RF Metamaterial Composite Based on Beam Focusing Transmitarray," *IEEE Antennas Wireless Propag. Lett.*, vol. 23, no. 6, pp. 1705-1709, June 2024.

[12] O. Bouvard *et al.*, "Mobile Communication Through Insulating Windows: A New Type of Low Emissivity Coating," *Energy Procedia*, vol. 122, pp. 781–786, Sep. 2017.

[13] H. Kim and S. Nam, "Transmission enhancement methods for low emissivity glass at 5G mmWave band," *IEEE Antennas Wireless Propag. Lett.*, vol. 20, no. 1, pp. 108–112, Jan. 2021.

[14] J. Chen *et al.*, "Transparent and broadband diffusion metasurface with high transparency and high shielding effectiveness using metallic mesh," *IEEE Trans. Antennas Propag.*, vol. 70, no. 7, pp. 5574–5583, Jul. 2022.

[15] A. Bagheri *et al.*, "Enhancing 5G Propagation into Vehicles and Buildings using Optically Transparent and Polarisation Insensitive Metasurfaces over Wide-Incidence Angles," *Sci. Rep.*, vol. 14, pp. 6832, 2024.

[16] S. Danesh *et al.*, "Wide-Incidence Angle and Polarisation Insensitive Transparent Metasurface for 5G Outdoor to Indoor Coverage Enhancement," *IEEE Antennas Propag. Soc. Int. Symp. (APSURSI)*, Denver, CO, USA, 2022.

[17] S. K. Sharma *et al.*, "A Micro Copper Mesh-Based Optically Transparent Triple-Band Frequency Selective Surface," *IEEE Antennas Wireless Propag. Lett.*, vol. 18, no. 1, pp. 202-206, Jan. 2019.

[18] H. Chen *et al.*, "Transparent FSS on Glass Window for Signal Selection of 5G Millimeter-Wave Communication," *IEEE Antennas Wireless Propag. Lett.*, vol. 20, no. 12, pp. 2319-2323, Dec. 2021.

[19] V. Singh *et al.*, "Fully transparent transmission surface for outdoor-indoor mmWave coverage enhancement," *Proc. Int. Conf. U.K.-China Emerg. Technol.*, Glasgow, U.K., pp. 1–4, 2020.

[20] G. Oliveri *et al.*, "Optically-Transparent EM Skins for Outdoor-to-Indoor mm-Wave Wireless Communications," *IEEE Access*, vol. 12, pp. 65178-65191, 2024.

[21] H. Miao *et al.*, "Sub-6 GHz to mmWave for 5G-Advanced and Beyond: Channel Measurements, Characteristics and Impact on System Performance," *IEEE J. Sel. Areas Commun.*, vol. 41, no. 6, pp. 1945-1960, June 2023.

[22] N. O. Oyie and T. J. O. Afullo, "Measurements and analysis of large-scale path loss model at 14 and 22 GHz in indoor corridor," *IEEE Access*, vol. 6, pp. 17205–17214, 2018.

[23] Y. Li *et al.*, "Path loss modeling for the RIS-assisted channel in a corridor scenario in mmWave bands," *Proc. IEEE Globecom Workshops (GCWkshps)*, Dec. 2022, pp. 1478–1483.

[24] B. Kim and J. Oh, "Single-Glass Layer Optically Transparent Transmitarray With High Aperture Efficiency And Low Profile At 5G Millimeter-Wave Band," *IEEE Trans. Antennas Propag.*, vol. 71, no. 11, pp. 9036-9041, Nov. 2023.

[25] G. Liu *et al.*, "A millimeter-wave multibeam transparent transmitarray antenna at Ka-band," *IEEE Antennas Wireless Propag. Lett.*, vol. 18, no. 4, pp. 631–635, Apr. 2019.

[26] D. Kitayama *et al.*, "Transparent dynamic metasurface for a visually unaffected reconfigurable intelligent surface: Controlling transmission/reflection and making a window into an RF lens," *Opt. Exp.*, vol. 29, no. 18, pp. 29292–29307, Aug. 2021.

[27] A. H. Abdelrahman *et al.*, "Transmission Phase Limit of Multilayer Frequency-Selective Surfaces for Transmitarray Designs," *IEEE Trans. Antennas Propag.*, vol. 62, no. 2, pp. 690-697, Feb. 2014.

[28] A. H. Abdelrahman, P. Nayeri, A. Z. Elsherbeni and F. Yang, "Bandwidth Improvement Methods of Transmitarray Antennas," *IEEE Trans. Antennas Propag.*, vol. 63, no. 7, pp. 2946-2954, July 2015.

[29] J. Yu, L. Chen, J. Yang and X. Shi, "Design of a Transmitarray Using Split Diagonal Cross Elements With Limited Phase Range," *IEEE Antennas Wireless Propag. Lett.*, vol. 15, pp. 1514-1517, 2016.

[30] B. Kim and J. Oh, "Characterization of Optically Transparent Two-Metal-Layered Refractive Metasurfaces for 6G Upper-Mid Outdoor-to-Indoor Communication," 2024 *IEEE AP-S/INC-USNC-URSI*, Firenze, Italy, 2024, pp. 1363-1364.

[31] A. Yu *et al.*, "Aperture efficiency analysis of reflectarray antennas," *Microw. Opt. Technol. Lett.*, vol. 52, no. 2, pp. 364-372, 2010.

[32] A. Bhattacharyya, Phased Array Antennas: Floquet Analysis, Synthesis, BFNs and Active Array Systems. Hoboken, NJ, USA: Wiley, 2006.

[33] S. H. Kang and C. W. Jung, "Transparent Patch Antenna Using Metal Mesh," *IEEE Trans. Antennas Propag.*, vol. 66, no. 4, pp. 2095-2100, Apr. 2018.

[34] C. Tian *et al.*, "A wideband transmitarray using triple-layer elements combined with cross slots and double square rings," *IEEE Antennas Wireless Propag. Lett.*, vol. 16, pp. 1561-1564, 2017.